Emergent Materials (2021) 4:1547–1557
https://doi.org/10.1007/s42247-021-00275-6

ORIGINAL ARTICLE

Non-destructive thickness measurement of thermal barrier coatings using terahertz radiation

Luis Isern[1] · Andrew J. Waddie[2] · Christine Chalk[1] · Andrew J. Moore[2] · John R. Nicholls[1]

Received: 3 May 2021 / Accepted: 21 July 2021 / Published online: 6 August 2021
© The Author(s) 2021

Abstract

A non-destructive thickness measurement technique based on terahertz (THz) reflectivity was successfully deployed to interrogate 7 wt.% yttria-stabilised zirconia thermal barrier coatings (TBCs) produced by electron-beam physical vapour deposition (EB-PVD). The THz technique was shown to produce accurate thickness maps for different samples with a resolution of 1 × 1 mm over a surface of 65 × 20 mm that were compared with direct examination of key cross-sections. All thickness measurements on different samples were calculated using a single value of refractive index. Small defects characteristic of EB-PVD, such as "carrot growths" and variations on column inclination, were evaluated and did not produce significant variations in the refractive index of the TBC. Moreover, the thickness maps correctly display thickness variations that are a consequence of the point-source nature of EB-PVD evaporation. In summary, this paper demonstrates the technique can be successfully deployed on large surfaces, and across different coatings of the same material produced under the same deposition conditions. It is shown that a single *n* value is required to map the thickness distribution for all samples. This combination of qualities indicates the potential of the technique for in-line control of TBC manufacture.

Keywords Terahertz imaging · Thermal barrier coatings · Electron-beam physical vapour deposition · Optical properties

1 Introduction

Thermal barrier coatings (TBCs) are highly engineered coating systems that enable aeroengines to operate at temperatures higher than the melting point of their structural materials [1, 2]. TBCs provide the thermal insulation that, combined with a sophisticated internal air-cooling system to extract the heat [3, 4], enable a thermal gradient of about 1 °C/μm between the coating surface and the nickel superalloy blade of the high-pressure, high-temperature turbine under a high energy flux of ~ 1 MW/m [5]. The required thermal gradient keeps increasing as the industry improves engine efficiency, in the drive to reduce carbon emissions, both of which demand higher operational temperatures [5]. TBCs are composed of several layers: a bondcoat that is applied on the metal substrate and provides an aluminium reservoir; a thermally grown oxide (TGO) made of alumina, from the oxidation of aluminium from the bondcoat, that reduces subsequent oxidation and improves the adhesion of the topcoat; and a ceramic topcoat that provides the thermal insulation and is usually based on yttria-stabilised zirconia (YSZ) [2, 5, 6]. For static parts of the engine, the ceramic is often deposited using a plasma spray technique, which produces a platelet structure with the lowest thermal conductivity. On the other hand, for moving parts such as turbine blades, electron-beam physical vapour deposition (EB-PVD) is preferred due to the formation of a columnar structure with better strain tolerance [2, 6]. Irrespectively of the deposition technique employed, control of coating thickness is key for component's performance due to the required balance between thermal insulation, excess weight and aerodynamic performance. For APS TBCs, any mismatch in thermal expansion, whether due to thermal gradients or variation in substrate material, leads to increased stress during thermal cycling; whereas for EB-PVD coatings that are strain tolerant, TBC mass and aerodynamic performance are critical; the former defines the centrifugal load on the component and

✉ Luis Isern
l.isernarrom@cranfield.ac.uk

[1] Surface Engineering and Precision Centre, Cranfield University, College Road, Cranfield MK43 0AL, Bedfordshire, UK

[2] Institute of Photonics and Quantum Sciences, Heriot-Watt University, Edinburgh EH14 4AS, UK

therefore creep behaviour, while the later defines the blades aerodynamic performance.

TBC manufacturing methods and practices heavily rely on destructive evaluation to measure TBC characteristics; bondcoat and ceramic microstructure, TGO and coating thickness and the TBC thickness variation around a blade profile. But this is at high costs, as single-crystal TBC-coated blades have to be destroyed. The associated cost provides a drive for a reliable non-destructive testing (NDT) technique to be developed. Currently, a number of NDT methods have been deployed on commercial TBC production to evaluate coating thickness, for example Eddie-current testing, weight gain and metrology techniques that include both mechanical and structured blue light scanning devices. However, their limitations mean that the use of destructive techniques is still predominant, such as the direct inspection of selected blade cross-sections. Sectioning requires the destruction of turbine blades at the very end of their production cycle: after single-crystal casting, laser drilling, surface preparation, multiple-stage bondcoat deposition and topcoat deposition, the destruction of a fully manufactured component represents a high commercial cost, especially for EB-PVD-coated turbine blades. THz frequency radiation has been proposed as an NDT technique to reduce or eliminate the need for destructive testing of high-value components because it can penetrate non-metallic dielectric materials, such as the topcoat and TGO, while reflecting off metals, such as the bondcoat. THz radiation illumination offers several advantages as it is non-ionising and can provide non-destructive, non-contact, real-time evaluation of the topcoat thickness and TGO growth [7, 8]. The thickness values obtained are precise, with most studies reporting error values of 1–5% [7–9]. An additional advantage is that THz techniques can be employed for in-service monitoring to track aging due to thermal-cycling (TGO growth and void formation) [10] and the effect of erosion [7]. Moreover, its application can be extended to other materials and coatings, provided that they are transparent to THz frequencies.

This paper describes the use of an alternative normal-incidence THz reflectivity technique [8] to measure the thickness of a number of 7 wt.% YSZ topcoat TBCs, produced from the same batch, using a single refractive index value. The THz measurements were taken by evaluating the reflectivity of the TBC to a high-power (5 mW) tuneable laser. The proposed technique combines high power and an intensity normalisation procedure to obtain well-formed reflectivity fringes that have an adequate signal-to-noise ratio to minimise the effect of water absorption lines [11]. This overcomes the need for the humidity control with time-domain spectroscopy (TDS) [7, 9, 10, 12], one of the main THz variants proposed, and makes it more suitable for in-line control applications because the distance between the emitter, sample and detector can be larger (~2 m for the present study). The proposed method measures the optical thickness, the combined effect of refractive index (n) and the thickness of the coating (t), returning $n*t$ values across the sample surface, and relies on the determination of a single n value to then calculate the thickness. This method has been described in detail on our previous publication [8]. In this paper, the study of this technique is expanded to analyse the effect of defects within the ceramic topcoat, and to test the effectiveness of using a single n value across different samples coated in the same deposition run. The proposed technique is also useful for the evaluation of coating aging in service conditions, which will be covered in subsequent publications.

2 Experimental methods

2.1 Coating deposition

Sample substrates were nickel alloy Nimonic® 75, machined to a dog-bone shape, 100 mm long and 36 mm wide. In previous experiments, similar dog-bones were pulled to investigate strain-induced birefringence in the TBC with GHz illumination [13, 14]: in the experiments reported in this paper, the dog-bones were not tensioned but were used to take advantage of existing mounts for the specimens during coating and the THz measurements. A β-NiAl bonding layer, 25–40 µm thick, was deposited onto grit-blasted substrates using Cranfield University's chemical vapour deposition facilities. For aging purposes that will be covered in a future publication, an intentional defect was introduced on the bondcoat of samples R1 and L1. The defect was created by masking-off the central region (around $x=0$ mm, $y=0$ mm, and of 5–10 mm in diameter) during the bondcoat deposition process to provide a region with low aluminium content. Finally, the aluminised samples were grit-blasted again and a ~300-µm-thick, 7 wt.% yttria-stabilised zirconia (7YSZ) layer was deposited using electron beam physical vapour deposition (EB-PVD) in Cranfield's custom-modified Electrotech CL680 vacuum coater (8 kW gun). The coater's loading chamber, described in Fig. 1a, can accommodate six substrates distributed around two triangular sample holders that are continuously rotated during deposition as per the figure. The long dimensions of the samples are laid perpendicular to the perspective of Fig. 1a and have a top–bottom orientation: top is closer to the viewer's perspective. Coating deposition took place at 1030 °C, in a 90% O_2/10% Ar atmosphere at $6 \bullet 10^{-3}$ mbar. The sample holders are designed to mask the end of the dog-bones and restrict the coating deposition to a narrower area of ~65 mm × 20 mm, as shown in Fig. 1b and c.

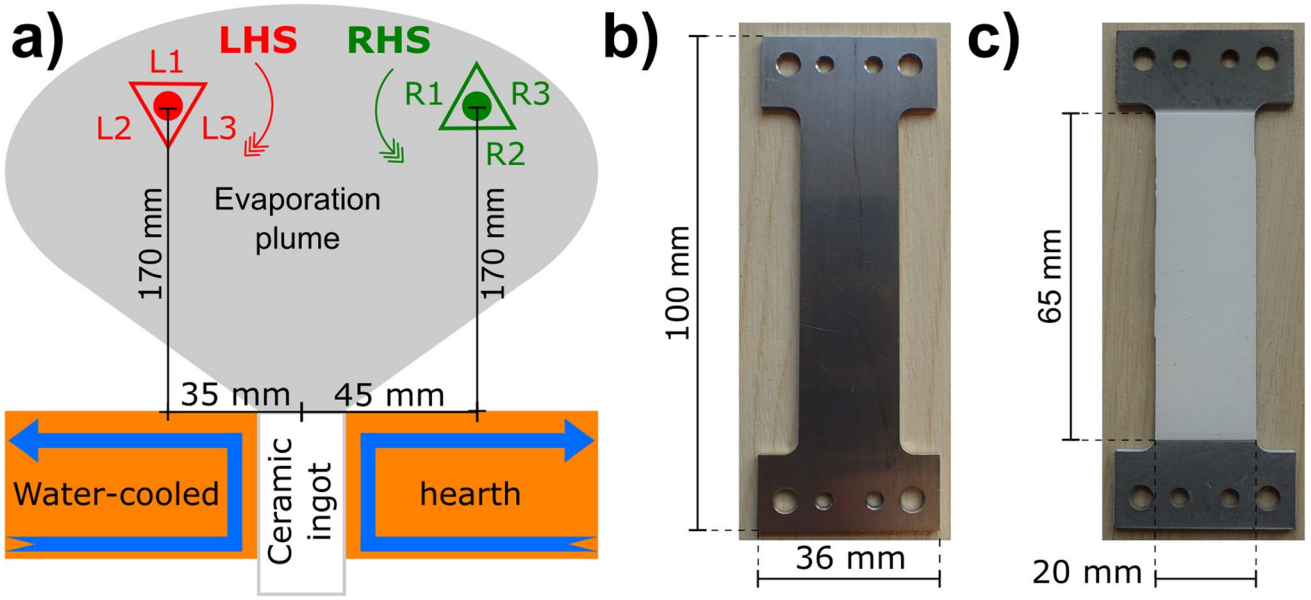

Fig. 1 **a** Schematic plan view of the EB-PVD deposition chamber where up to three samples can be mounted on each holder (left-hand side — LHS for samples L1, L2, L3, and right-hand side — RHS for samples R1, R2, R3). The dog-bones are mounted to the sample holder with their long dimension perpendicular to the plane of the schematic. Image of dog-bone substrates **b** before and **c** after TBC deposition (bondcoat and 7YSZ)

2.2 THz experimental setup

Figure 2 presents a schematic of the THz experimental setup. The THz idler beam output, produced by the M2 Firefly OPO, under pump illumination supplied by the 1064 nm M2-ICE laser, is passed through a linear polariser (P1) to ensure that the illumination entering the system is vertically polarised. Due to the observed ~ 10% pulse-to-pulse THz intensity variation, the near-IR signal beam from the OPO was monitored by an InGaAs photodiode (PD) to allow compensation for this variation to be made. Each measurement point presented in this paper is the average of 50 pulses to further

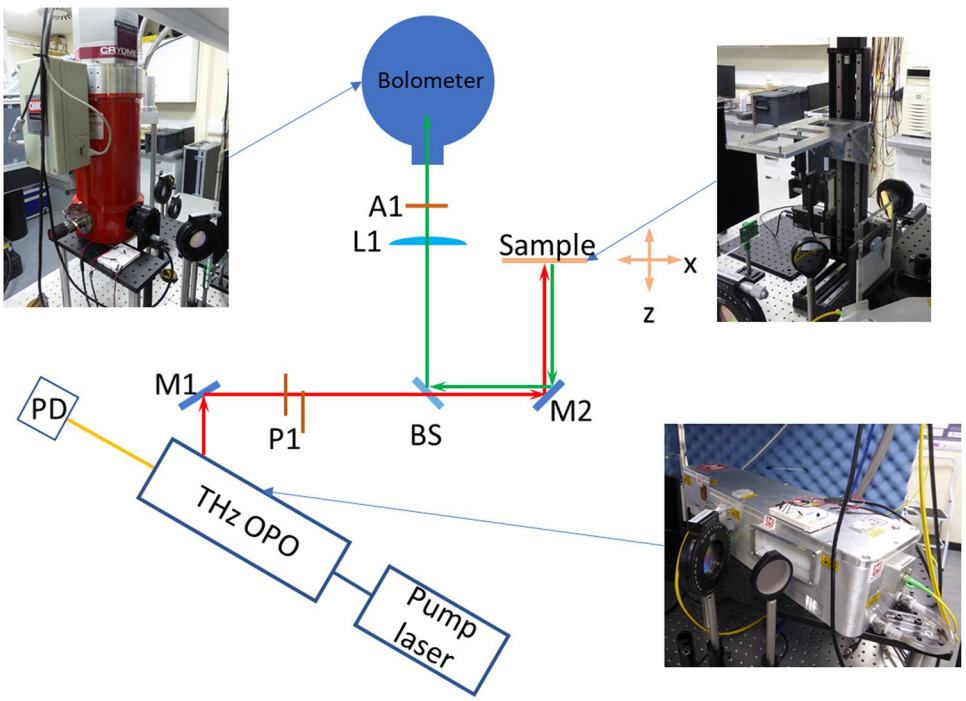

Fig. 2 Schematic of experimental setup. M1, flat mirror; P1, linear polariser; BS, Si beam splitter; M2, parabolic mirror; L1, PTFE lens; A1, linear analyser; PD, photodiode

improve the overall SNR of the data. The parabolic mirror M2 ($f = 152.4$ mm) focuses the incident THz beam (shown in red) on to the sample and the reflected beam (shown in green) is then transmitted back along the incident beam path and reflected by the Si beam splitter (BS) into the detection arm of the instrument. The PTFE lens L1 ($f = 100$ mm) is then used to focus the reflected THz beam onto the THz detector. In this paper, a cyrostatically cooled superconducting bolometer (QMC Instruments Ltd QNbTES/X) was used but the Firefly system is of sufficient brightness that a lower-specification detector, such as a pyrometer, could equally well be used. The sample is translated in *X*, *Y* and *Z* directions by means of a set of motorised translation stages (Zaber Technologies Inc. X-LRQxxxBL-E01; x-,y- 450 mm; z- 75 mm) allowing a scan of the whole sample to be made at a maximum resolution corresponding to the measured focal spot diameter of 1 mm on the TBC specimen. Currently, the overall measurement speed of the system is relatively slow due to the low repetition rate of the THz laser (50 Hz), the need to mechanically translate the samples with each translation point taking approximately 1.5 s and each of the four frequencies approximately 1 s, and the large amount of measuring points (1,200 per sample), leading to a total measurement time per sample of around 5 h.

2.3 Thickness measurement

The optical thickness is determined by combining a thin film model fit of the measured reflectivity spectrum at a small number of points across the sample with a higher spatial resolution measurement using the Carré phase stepping method. Both the thin film model, which can include multiple layers and surface roughness, and the Carré phase stepping method, which is needed to remove the observed n^*t indeterminacy of the thin-film model, were described in detail in our previous publication [8]. The optical thickness determination required two separate measurements on the sample: the first, needed for the thin-film model fit, recorded the full reflectivity spectrum between 1.2 and 1.6 THz at points on a 7-mm grid; the second, needed for the Carré phase stepping, measured the reflectivity at four discrete frequencies (1.255,1.285,1.315 and 1.345 THz) at points on a 1-mm grid.

The coating thickness was verified by direct optical microscopic inspection. One sample was cut along seven transversal sections, starting from the centre of the coated area and then at intervals of $+7, +14, +21$ and $-7, -14, -21$ mm either side of the centre ($y = 0$ mm) as shown in Fig. 3 (black lines). Samples were maintained in the same orientation throughout the experiments, with the orientation up-down being consistent for all samples and determined by the specimen orientation in the sample holder during deposition. A resin was applied to the TBC coating prior to mounting and polishing of the cross-sections to avoid damage to the TBC column tips. Samples were inspected using a digital microscope (optical) Keyence VHX6000. Thickness measurements were taken using Keyence's software every mm, on points that coincided with THz measurements (Fig. 3, red lines). The TBC images presented in this article were taken using the back-scattered detector of a TESCAN Vega 3 scanning electron microscope (SEM) at 20 kV, working distance of 10 mm and spot size of 68 nm; cross-sections were previously coated with 10 nm of gold to enhance image resolution.

3 Results

Six thermal barrier–coated dog-bones were produced for this study: three on the right-hand side holder, labelled R1, R2 and R3, and three on the left-hand side holder, labelled L1, L2 and L3 (numbering is arbitrary). TBC thickness inspection by THz radiation was performed in all samples as detailed in the previous section.

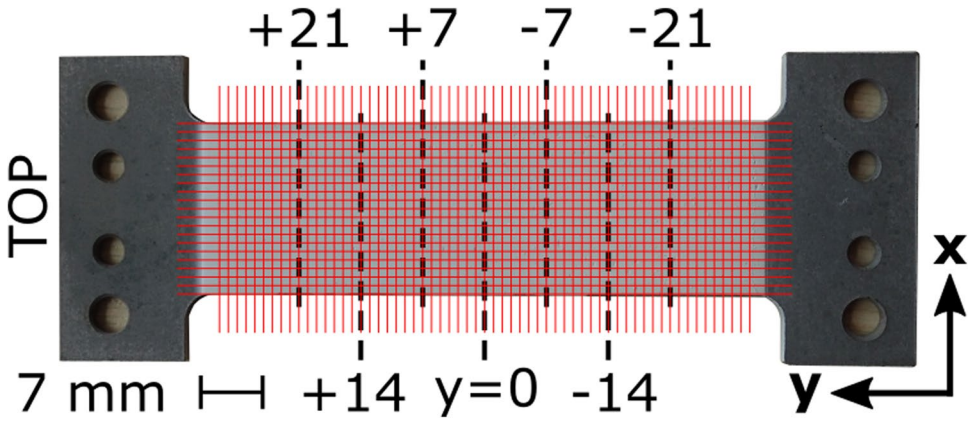

Fig. 3 Dog-bone sample image with superimposed thickness measurement points. Thick black discontinuous lines correspond to transversal cross-sections cut for optical microscopy (every 7 mm from $y = 0$) with their nomenclature. The intersection of thin red lines marks THz measurement points (every 1 mm). Regarding orientation, longitudinal direction corresponds to *y* axis and transversal to *x* axis

3.1 Thickness validation

Sample R2 was selected as a reference sample to validate the THz technique for thickness measurement. R2 was physically sectioned at 7-mm intervals transversally as per Fig. 3 and inspected by optical and electronic microscopy. Representative examples of the cross-sections are shown in Fig. 4, where back-scattered SEM imaging reveals atomic number contrast of the distinct coating layers of the TBC. All images show the columnar microstructure of the TBC growing on the thin Al_2O_3 oxide (thin black line, < 2 µm thickness), which in turn is on top of a ~ 25-µm β-NiAl layer that appears slightly darker than the underlying Nimonic75® substrate. The thickness of the TBC is relatively homogeneous and there are no major defects present, except for the occasional minor defects known as "carrot growths", 50–300 µm wide, which are discussed in detail in a later section. The "carrot growths" are produced during regular evaporation in EB-PVD and their presence is tolerated if small-sized and in small quantities. The columns nucleate very finely at the bondcoat interface but grow much wider towards the coating surface. Column inclination changes perceptibly across the longitudinal direction of the sample. Columns in sections $y = +21$ and $+14$ mm (i.e. near the "top" of the sample) are almost perfectly parallel to the *xz*-plane of the cross-section and the full columns are shown in their entirety (Fig. 4a and b). Near the "bottom" of the sample, the columns have some perceptible tilt with respect to the plane of the cross-section at $y = 0$ mm (Fig. 4c), and this is much more accentuated at $y = -21$ mm where the column intersections with the polished cross-section now appear as small ellipses (Fig. 4d). This variation in the growth direction of the columns is due to the expansion of the evaporation plume and is discussed further in a later section.

The central point of Sect. 0 mm (the central cross-section) was taken as a reference for the thickness calibration. At this point, the thickness was measured at 287 ± 5 µm from optical microscopy, and the value of n^*t (the THz optical thickness) was 1,140 ± 20 µm, which corresponds to a TBC refractive index to THz radiation of 3.977. This refractive index was used for the calculation of the thickness from the THz measurements in the rest of this sample and for the other samples in this study.

At each transversal section, optical microscopic measurements were taken every 1 mm, the same spatial resolution as THz imaging. The microscopic measurements mostly agree with the thickness curves calculated from THz radiation as shown in Fig. 5. The experimental error considers both the limitations of the measuring device, positioning and the peak-to-valley distance of the columns at the surface. Less than 5% of THz measurement points fall outside the error bars of the microscopic measurements; these are mostly related to "carrot growth" defects and are explained in a subsequent section. Moreover, the graphs reveal different trends for the longitudinal and transversal directions on the samples. Longitudinally, the thickness fits a spherical shape with an absolute maximum at around section $y = +5$ mm. Transversally, the

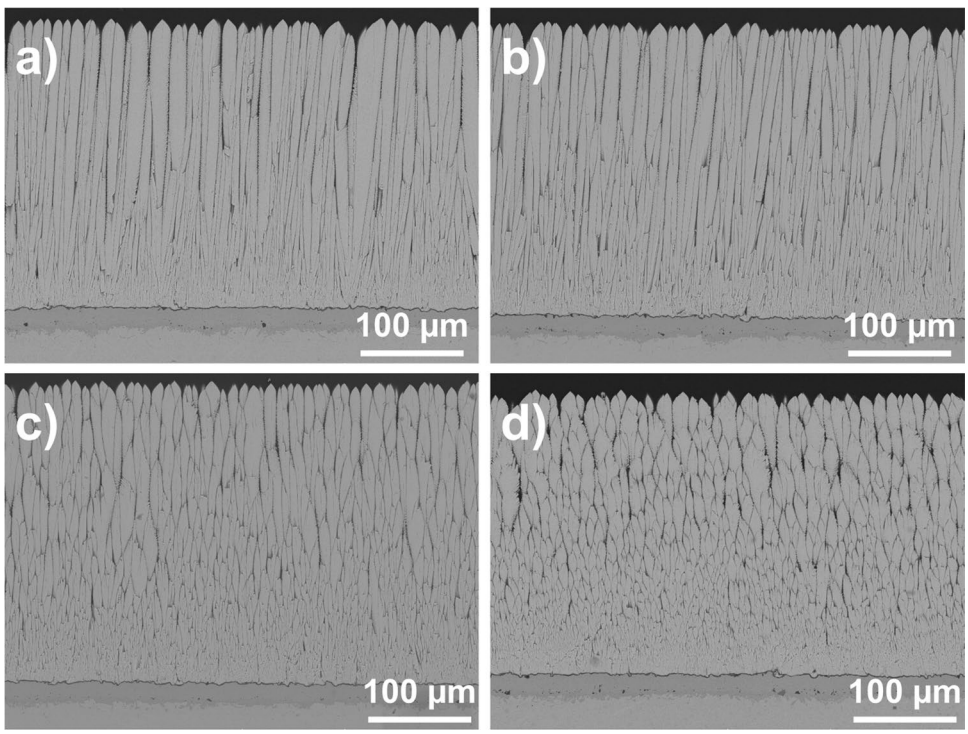

Fig. 4 TBC images from sample R2 at *y*-sections of **a** + 21 mm, **b** + 14 mm, **c** 0 mm and **d** − 21 mm

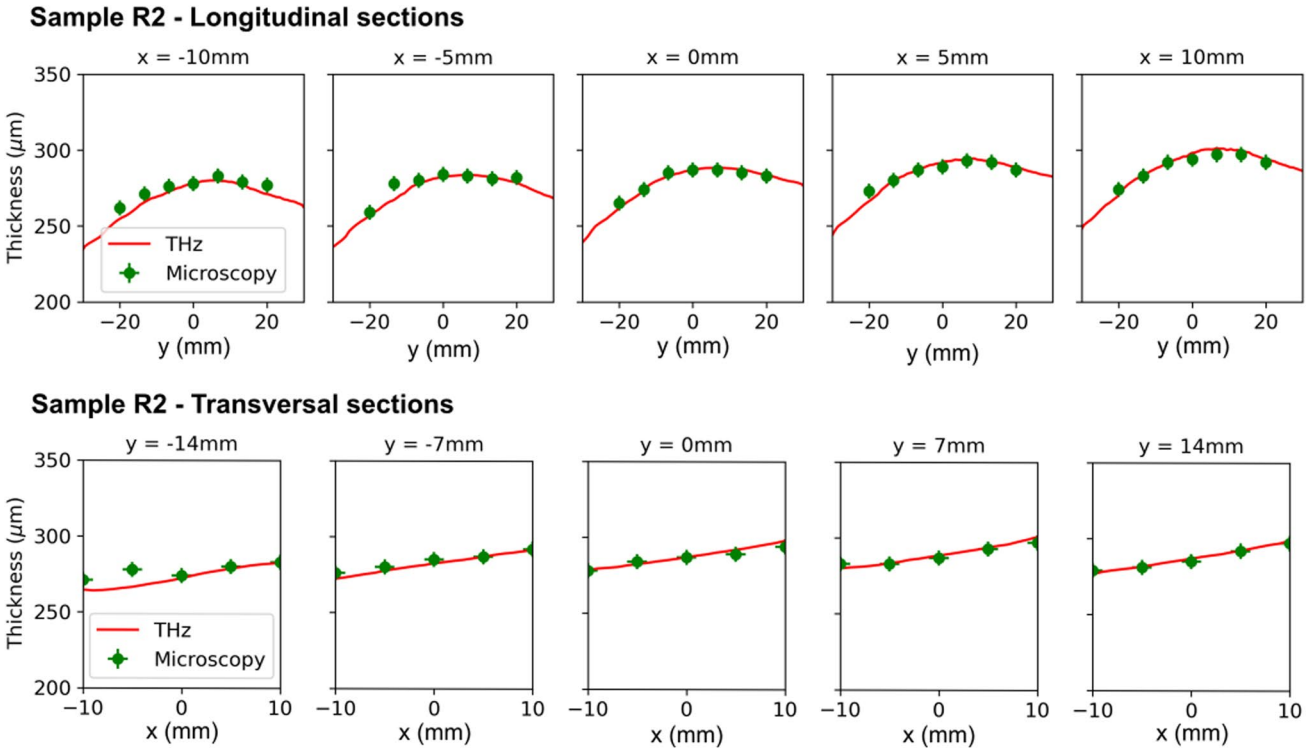

Fig. 5 Comparison of thickness measurements by microscopical inspection of cross-sections (green dots) with THz imaging calculations (red curves) for longitudinal sections at different x positions, and transversal sections at different y positions on sample R2. Microscopic measurements are only plotted every 5 mm on the transversal sections to enhance clarity

thickness increases from left to right. Both trends are related to the "point-source evaporator" characteristic nature of the EB-PVD deposition as reviewed in the discussion.

Sample L2 was also sectioned to validate THz thickness measurements, calibrated using the refractive index from sample R2. In this case, sectioning happened after the sample had been thermally cycled between room temperature and 1100 °C for 20 × 1-h cycles with a short period of forced air cooling, to study the impact of aging to be reported in a further publication. The microstructure of the coating has been little altered for the short thermal cycling and both THz and direct inspection thickness measurements seem unaffected by this cyclic heat treatment. The results from both measurement techniques are in agreement (Fig. 6), which demonstrates that THz imaging using a single refractive index can be used to estimate TBC thickness on the same coating batch. The main source of disagreement (error) between microscopy and THz measurements is due to "carrot growth" defects, as detailed in the subsequent section "3.3. Effect of defects".

3.2 Thickness maps

Reflectivity maps of all samples were obtained using four discrete frequencies (1.255, 1.285, 1.315 and 1.345 THz). Applying the previously obtained refractive index of 3.977, the reflectivity maps can be converted into thickness maps as shown in Fig. 7. These maps reveal a strong handedness of the samples, with all R samples having the local maximum on the right-hand side, whereas all L samples having the local maximum on the left-hand side. This is explained by the direction of rotation of the samples, described in Fig. 1, and their orientation on the holder, perpendicular to the Fig. 1 schematic and considering the sample "top" as closer to the point of view of the reader. The leading edge (i.e. the foremost edge on the direction of rotation) of L samples is the left-hand side, whereas for R samples is the right-hand side. Therefore, the local-maximum side is the leading-edge, as expected. Longitudinally, this local maximum occurs at approximately $y = +5$ mm as noted previously, which corresponds to the small vertical offset of the ceramic ingot with respect to the rotating sample holders. The minimum thickness is located on the bottom corner opposite to the maximum (trailing-edge of the rotation), and the thickness variation across each sample is ~ 40 μm. Samples coated on the left-hand side holder have a greater thickness across their whole surface, which is expected due to the asymmetric position of the two substrate holders in the chamber with the left being closer

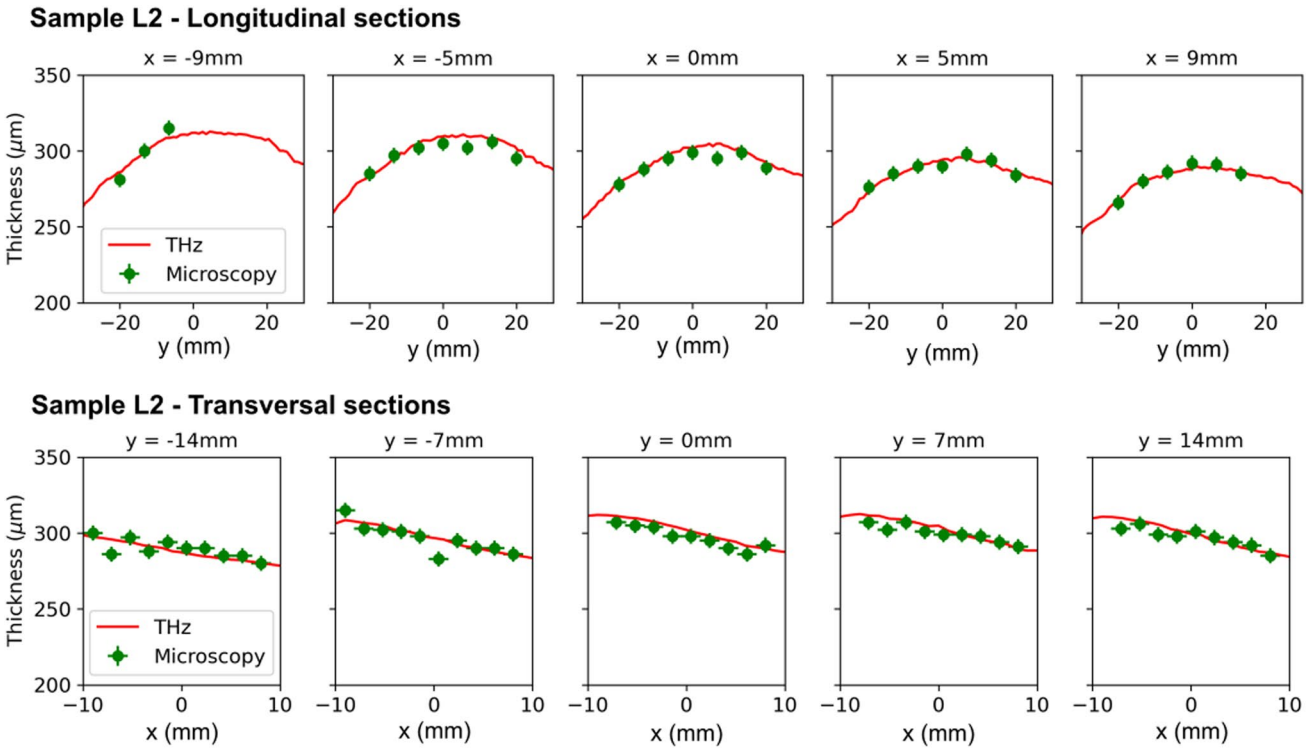

Fig. 6 Comparison of thickness measurements by microscopical inspection of cross-sections (green dots) with THz imaging calculations (red curves) for longitudinal sections at different x positions, and transversal sections at different y positions on sample L2. Only half of the microscopic measurements are plotted on the transversal sections to enhance clarity. Some longitudinal sections near the edges of the sample ($x = -9$ and $+9$ mm) miss points of microscopical inspection due to chipping on the sample edges after the heat treatment cycles

to the ingot (Fig. 1). There seem to be small thickness variations within the L samples, as well as within the R samples, with L3 and R2 being the thickest of the groups. This is likely a consequence of the holders not being perfectly horizontal, so one of the faces of the triangle is closer to the ingot. In summary, the thickness distribution on the samples corresponds well with the distance

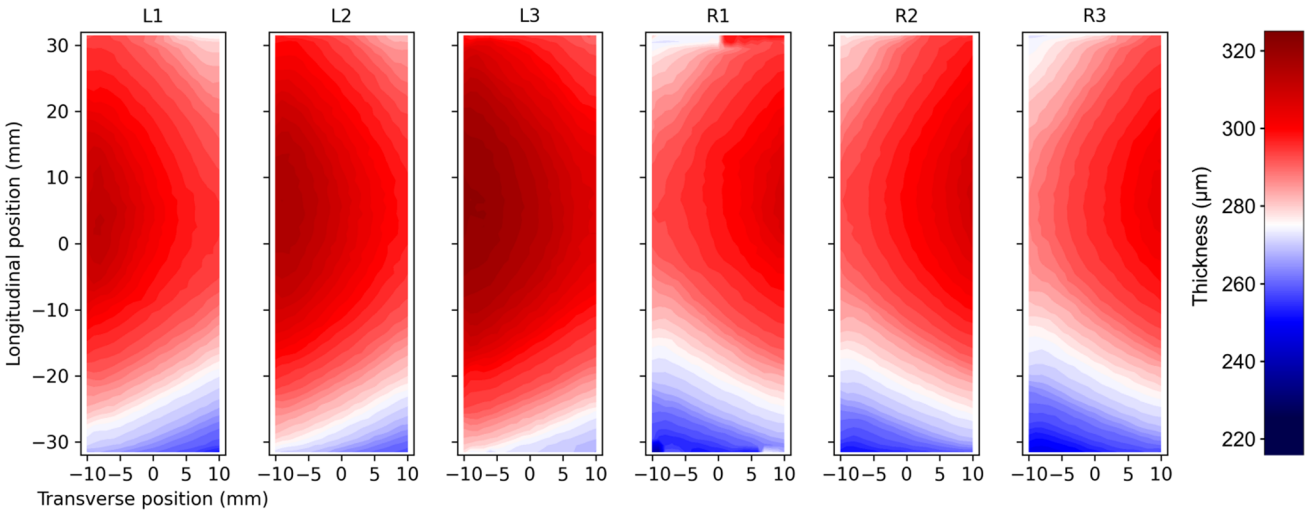

Fig. 7 Thickness maps for all samples constructed from THz reflectivity measurements. Each sample (R1, R2, R3 and L1, L2, L3) is labelled above the corresponding thickness map

to the ingot and the direction of rotation, as predicted by a "point source" evaporation model.

3.3 Effect of defects

There are no major defects present within the ceramic layer of the studied TBCs. Some minor defects produced by the nature of EB-PVD deposition are present, but do not seem to affect THz mapping. One example of such defects is the clusters of thicker columns known as "carrot growth" defects, as illustrated in Fig. 8. These are associated with local re-nucleation on a foreign particle that are produced in small numbers as part of nominal EB-PVD evaporation. The "carrot growths" are usually 50–300 µm in diameter and comprise multiple columns; hence, they are smaller than the ~ 0.5 by 1.0 mm diameter irradiated by the THz laser. Consequently, THz measurements give the average of the thickness across the irradiated area and do not resolve "carrot growths". By contrast, direct examination of the cross-sections produces point measurements at a given position that are affected by the local presence of "carrot growths". As observed in Fig. 8d, some "carrot growths" can be up to 100 µm taller than the average of neighbouring columns. Moreover, the presence of a tall "carrot growth" creates a shadow around it, partially masking neighbouring columns and reducing their growth as seen in Fig. 8d. This shadowing effect also produces some discrepancies where direct observation produces lower values than THz counterparts, such as the low outlier in $(x, y) = (0, -7)$ in Fig. 6. In general, discrepancies between direct observation and THz radiation correspond to local effects of "carrot growths".

Another minor defect is the change in column inclination across the length of the sample, as observed in Sect. 3.1. The inclination is related to the relative position of the sample with respect to the ingot being evaporated. This does not seem to affect the value of n, deduced through the good agreement of the THz thickness maps and the cross-sections (Fig. 5).

Finally, the bondcoat of four samples (R1 and L1) had an intentional defect around the central area, as described in the methodology. It is noted that the thickness maps of those samples (Fig. 7) are not influenced by the presence of these macro-defects. The THz radiation, at the current frequencies used, is reflected by the metallic nature of the bondcoat and therefore does not see these bondcoat defects. Therefore, the defect induced in the bondcoat (which results in aluminium deficiency) does not change its metallic nature and hence does not affect its reflectivity. The only effect that THz radiation could detect is changes in the thermally grown oxide (TGO). However, the TGO thickness of all samples examined is too small (<2 µm) after this short time of aging to show any effect on the thickness maps.

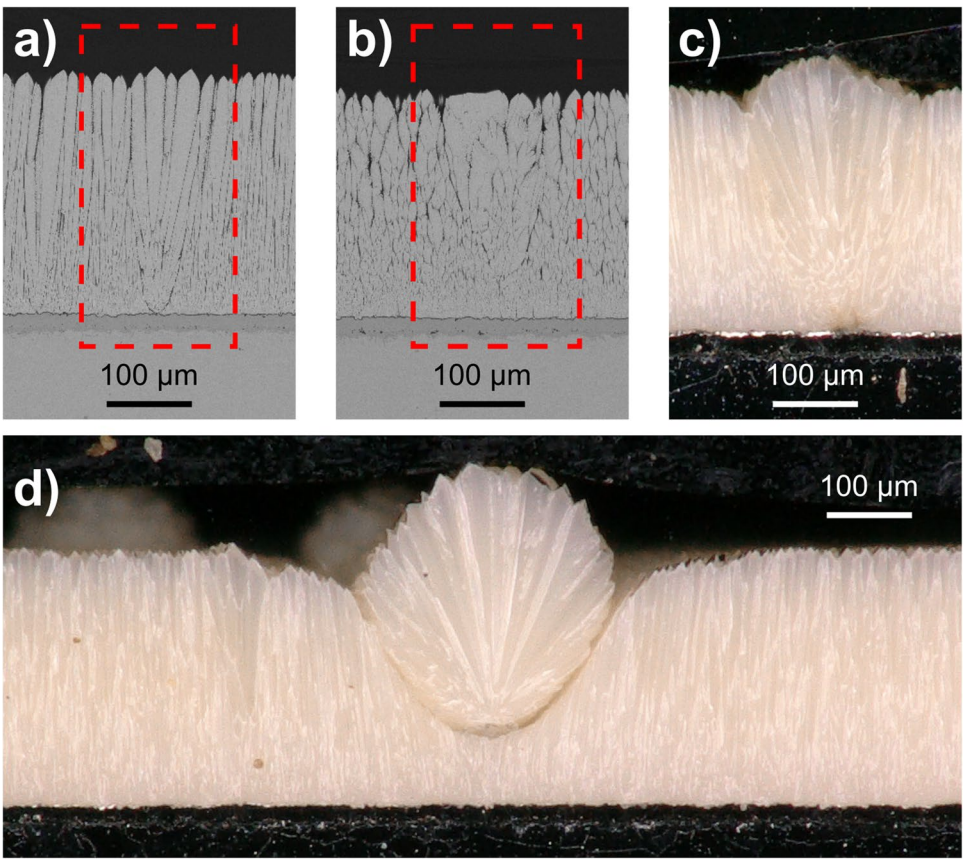

Fig. 8 **a** and **b** Cross-sectional back-scattered SEM image from sample R2 highlighting "carrot growth" defects. **c** and **d** Dark field digital microscope images of "carrot growths" in sample L2

4 Discussion

THz imaging demonstrates to be an accurate non-destructive method to map TBC thickness. The method followed here consists of measuring the $n*t$ value by THz imaging an area and then obtaining n by measuring the coating thickness by direct inspection of one cross-section on a calibration sample. This single n value is used to estimate the coating thickness from $n*t$ measurements in other parts of the sample and other samples manufactured at the same time. The use of a single n value was successfully trialled on 7YSZ, covering smaller areas of about 25 mm in diameter, for plasma-sprayed [7, 12] and EB-PVD [9] coatings with THz time domain spectroscopy, and was also briefly reported by us for the new THz technique [8]. The current publication addresses the concern that variations in the microstructure arising from specifics of the coating production might affect the refractive index of the coatings: a single n value was successfully used in the presence of variations in column inclination, defects and after thermal aging.

In principle, THz imaging could be deployed as a non-destructive technique for quality control during the manufacturing process of TBCs on industrial scale. Our results show that the method is reliable within a sample (Fig. 5) and within a coating batch (Figs. 6 and 7). This is because any changes in the refractive index caused by column inclination and other minor defects such as "carrot growth" defects are too small to affect the thickness measurement by THz radiation. Moreover, the THz method averages the thickness of the area irradiated, which is less sensitive to the presence of "carrot growths" (Fig. 8) and even column tip variation than direct inspection of the cross-section. Potentially, this method could be applied to batches of samples produced using the same coating technique and deposition conditions, perhaps with the use of one sample per batch to correct for variations in the refractive index value. However, this method cannot be applied as a universal solution, using a single n value, for coatings produced by different deposition methods and with different parameters, because the refractive index is too sensitive to larger variations in coating microstructure. For example, the difference between EB-PVD columns and plasma-sprayed splats is significant: at similar THz frequencies, the refractive index obtained here (3.977) is similar to other EB-PVD 7YSZ coatings measured in the literature (3.73 [9]), but is smaller than for plasma-sprayed 7YSZ coatings, which are in the range of 4.0–5.2 [7, 10, 12, 15]. Even for coatings deposited using the same deposition technique, other factors, such as porosity, stress or density, affect the value of n. Watanabe et al. [15] studied the effect of porosity on plasma-sprayed 7YSZ coatings and concluded that the refractive index changed inversely with porosity, from 5.7 for a fully sintered sample to 4.0 for the most porous coating. A similar range was found by Fukuchi et al. [12] also for plasma-sprayed coatings who, in addition, studied bulk 7YSZ at different stages of sintering which rendered values between 4.6 and 5.2.

The 65 × 20 mm area inspected here is large enough to investigate and analyse features that are characteristic of EB-PVD deposition, such as the consistent variation in thickness with change in distance from the source. It has been long understood that the evaporation can be approximated as a "point-source" deposition process [16] with some local vapour scattering; thus, the thickness distribution depends on distance from the source and the inclination angle from the source normal, i.e. from the vertical [17]. Therefore, the handedness of the thickness results identified in Fig. 7, the maximum thickness value around the + 5 mm Y position, and the larger thicknesses of left-hand side samples are all as expected and a consequence of the point-source nature of EB-PVD evaporation. By analogy, the non-uniform coating thicknesses that arise due to variations in the local deposition angle caused by substrate curvature could also be measured. Current industrial practice compensates this effect by using different rotational speeds in different parts of each revolution; the technique presented on this paper could be applied to track the thickness profile in-line, which would enable immediate adjustment of the different rotational speeds to achieve a more uniform coating. The upper limit of measurement area is only restricted by practicalities of presenting the instrument to the coating and the total time required to measure at all points of interest.

Previous studies on the effect of TBC defects on THz imaging have focused on the bondcoat and thermally grown oxide (TGO) rather than on the ceramic layer. Chen et al. [10] concluded that THz imaging is able to monitor the evolution of the TGO growth and void formation, which is of paramount importance to the coating's life in service. However, any damage introduced by thermal oxidation in the work of Chen et al. (1350 h at 1100 °C) falls outside of the scope of the present publication. In this study, the bondcoat defect induced in specific samples would cause an in-service modification to the TGO composition in the affected area, where the lack of available aluminium will lead to the formation of less protective oxides (chromia, nickel oxide…) rather than α-alumina as found on the rest of the sample. This change in oxidation effect was not detected in the present samples, when the TGO could not grow more than 1–2 μm; hence, no differences were detected on the maps of Fig. 7. Defects to the ceramic layer have not been studied in detail by THz imaging, apart from the mentioned effect of porosity. Ye et al. [7] studied the effect of 7YSZ surface roughness and also erosion of the 7YSZ layer, although the erosion was only reported as a difference

in thickness values. To the best of the authors' knowledge, no other studies have been reported in the literature on the effect of ceramic defects, such as "carrot growth" defects or column inclination. This may be due, in part, to the inspection of small areas reported in previous publications, where variations such as column inclination are not a significant factor. It is likely that the wide area covered by the laser-source (~0.5 by 1.0 mm in diameter) can average out the presence of smaller defects that are 50–300 μm in diameter. In a similar manner, the column inclination will not change the overall porosity of the coating so its effects may also be averaged out by the large laser-source.

Finally, the error induced by THz imaging is small and in line with current experimental techniques, such as direct optical inspection of cross-sections. All of the published studies that studied thickness discrepancies and systematic error agree on attributing an error value in the range of 1–5% [7–9]. Our THz technique overcomes the need for strict humidity control and enables a relatively large stand-off distance to the specimen, which could make implementation for quality control more straightforward. This paper establishes the principles of THz imaging for thickness measurement of thermal barrier coatings. Clearly, a large amount of research and development is required to develop a suitable instrument for quality control applications, which will be the subject of future work.

5 Conclusions

A non-destructive method for thickness measurement of TBCs has been developed based on terahertz imaging. The proposed method uses a single refractive index to estimate the thickness across a whole sample and for coatings of the same evaporation batch, overcomes the need for strict humidity control, and enables a relatively large stand-off distance to the specimen. Maps detailing the coating thickness of a 65 × 20 mm area have been produced for six samples and the accuracy of this method has been successfully validated by direct inspection. The results presented here reveal the potential of this method as a quality control tool for detailed, accurate, non-destructive measurement of TBCs and other ceramic coatings that can be penetrated by THz illumination.

Acknowledgements This work was funded by the Engineering and Physical Sciences Research Council under grants EP/N018141/1 and EP/N018249/1; plus additional technical support from Renishaw plc.

Further, the authors wish to acknowledge the invaluable contribution of Tony Gray (Senior Technical Officer) at Cranfield University for his work in the production of the TBC samples.

Author contribution All authors contributed to formal analysis and investigation, methodology, and manuscript review and editing. Original draft and original figures produced by L Isern and AJ Waddie. Data acquired and samples prepared by L Isern, C Chalk and AJ Waddie. Funding acquired by AJ Moore and JR Nicholls.

Funding This work was funded by the Engineering and Physical Sciences Research Council under grants EP/N018141/1 and EP/N018249/1; plus additional technical support from Renishaw plc.

Availability of data and material The manuscript contains all necessary data. Further material will be provided upon request by the corresponding author.

Code availability Not applicable.

Declarations

Conflict of interest The authors declare no competing interests.

Open Access This article is licensed under a Creative Commons Attribution 4.0 International License, which permits use, sharing, adaptation, distribution and reproduction in any medium or format, as long as you give appropriate credit to the original author(s) and the source, provide a link to the Creative Commons licence, and indicate if changes were made. The images or other third party material in this article are included in the article's Creative Commons licence, unless indicated otherwise in a credit line to the material. If material is not included in the article's Creative Commons licence and your intended use is not permitted by statutory regulation or exceeds the permitted use, you will need to obtain permission directly from the copyright holder. To view a copy of this licence, visit http://creativecommons.org/licenses/by/4.0/.

References

1. H. Xu, H. Guo, S. Gong, 16 - Thermal barrier coatings. Developments in high-temperature corrosion and protection of materials. (2008), pp. 476–491. https://doi.org/10.1533/9781845694258.2.476
2. J.R. Nicholls, Advances in coating design for high-performance gas turbines. MRS Bull. **28**(9), 659–670 (2003). https://doi.org/10.1557/mrs2003.194
3. K.G. Kyprianidis, Future aero engine designs: an evolving vision. Advances in Gas Turbine Technology. (2011). https://doi.org/10.5772/19689
4. M. Kawamura, Y. Matsuzaki, H. Hino, S. Okazaki, Evaluation of graded thermal barrier coating for gas turbine engine. Functionally graded materials 1996. (Elsevier Science B.V., 1997), pp. 413–418. https://doi.org/10.1016/B978-044482548-3/50068-8
5. D.R. Clarke, M. Oechsner, N.P. Padture, Thermal-barrier coatings for more efficient gas-turbine engines. MRS Bulletin. **37**(10), 891–898 (2012). https://doi.org/10.1557/mrs.2012.232
6. R. Darolia, Thermal barrier coatings technology: critical review, progress update, remaining challenges and prospects. International Materials Reviews. **58**(6), 315–348 (2013). https://doi.org/10.1179/1743280413Y.0000000019
7. D. Ye, W. Wang, J. Huang, X. Lu, H. Zhou, Nondestructive interface morphology characterization of thermal barrier coatings using terahertz time-domain spectroscopy. Coatings. **9**(2), (2019). https://doi.org/10.3390/COATINGS9020089
8. A. Waddie, P. Schemmel, C. Chalk, L. Isern, J. Nicholls, A. Moore, Terahertz optical thickness and birefringence

measurement for thermal barrier coating defect location. Optics Express. **28**(21), 31535–31552 (2020). https://doi.org/10.1364/OE.398532
9. J. White, G. Fichter, A. Chernovsky, J.F. Whitaker, D. Das, T.M. Pollock, et al, Time domain terahertz non-destructive evaluation of aeroturbine blade thermal barrier coatings. AIP Conference Proceedings. (American Institute of Physics, 2009), pp. 434–439. https://doi.org/10.1063/1.3114273
10. C.-C. Chen, D.-J. Lee, T. Pollock, J.F. Whitaker, Pulsed-terahertz reflectometry for health monitoring of ceramic thermal barrier coatings. Optics Express. **18**(4), 3477 (2010). https://doi.org/10.1364/oe.18.003477
11. J. Tennyson, P.F. Bernath, L.R. Brown, A. Campargue, A.G. Császár, L. Daumont, et al, A database of water transitions from experiment and theory (IUPAC technical report). Pure Appl. Chem. **86**(1), 71–83 (2014). https://doi.org/10.1515/pac-2014-5012
12. T. Fukuchi, N. Fuse, M. Okada, T. Fujii, M. Mizuno, K. Fukunaga, Measurement of refractive index and thickness of topcoat of thermal barrier coating by reflection measurement of terahertz waves. Electronics and Communications in Japan. **96**(12), 37–45 (2013). https://doi.org/10.1002/ecj.11551
13. P. Schemmel, G. Diederich, A.J. Moore, Direct stress optic coefficients for YTZP ceramic and PTFE at GHz frequencies. Optics Express. **24**(8), 8110 (2016). https://doi.org/10.1364/OE.24.008110
14. P. Schemmel, G. Diederich, A.J. Moore, Measurement of direct strain optic coefficient of YSZ thermal barrier coatings at GHz frequencies. Optics Express. **25**(17), 19968 (2017). https://doi.org/10.1364/OE.25.019968
15. M. Watanabe, S. Kuroda, H. Yamawaki, M. Shiwa, Terahertz dielectric properties of plasma-sprayed thermal-barrier coatings. Surf. Coat. Technol. **205**(19), 4620–4626 (2011). https://doi.org/10.1016/j.surfcoat.2011.03.144
16. J.A. Thornton, High rate thick film growth. Annu. Rev. Mater. Sci. **7**(1), 239–260 (1977). https://doi.org/10.1146/annurev.ms.07.080177.001323
17. E.B. Graper, Distribution and apparent source geometry of electron-beam-heated evaporation sources. Journal of Vacuum Science and Technology **10**, 100–103 (1973). https://doi.org/10.1116/1.1317914

https://dspace.org/

Non-destructive thickness measurement of thermal barrier coatings using terahertz radiation

Isern, Luis; Waddie, Andrew J.; Chalk, Christine; Moore, Andrew J.; Nicholls, John R.

2021-08-06
Springer
https://doi.org/10.1007/s42247-021-00275-6
Isern L, Waddie AJ, Chalk C, et al., (2021) Non-destructive thickness measurement of thermal barrier coatings using terahertz radiation. Emergent Materials, Volume 4, Issue 6, December 2021, pp. 1547–1557

Downloaded from a DSpace repository. https://dspace.org/